Combustion Theory and Modelling, 2023
Vol. 27, No. 1, 103–117, https://doi.org/10.1080/13647830.2022.2153741

Comparison of combustion duration and end-gas autoignition in inwardly and outwardly propagating flames induced by different ignition configurations

Linlin Yang, Yiqing Wang and Zheng Chen *

SKLTCS, CAPT, College of Engineering, Peking University, Beijing, People's Republic of China

(*Received 25 April 2022; accepted 15 November 2022*)

Recently, multiple spark ignition has received great attention since it helps to increase thermal efficiency and to reduce misfire in engines. Multiple spark ignition also affects the combustion duration and thereby it can be used for knock control. However, previous studies reported opposite trends in terms of how multiple spark ignition affects engine knock. This work aims to assess and interpret the influence of flame propagation direction induced by different ignition configurations on combustion duration and end-gas autoignition/engine knock. Two simplified and idealised ignition configurations are studied theoretically and numerically. One is with infinite number of sparks at side circular wall, which induces an inwardly propagating flame (IPF); and the other is with a single central spark, which induces an outwardly propagating flame (OPF). In the asymptotic theoretical analysis, the canonical 1D formulations for IPF and OPF are reduced to 0D model. Based on the 0D model, OPF and IPF at different initial temperatures are studied and compared. Counterintuitively, it is found that the combustion duration of OPF is shorter than that of IPF when there is no end-gas autoignition. On the other hand, the combustion duration of IPF is shorter than that of OPF when end-gas autoignition occurs. Furthermore, end-gas autoignition is found to be more prone to occur in IPF than OPF. These interesting observations are interpreted through assessing the ignition delay time and different components of the absolute flame propagation speed. The theoretical results are validated by transient simulations considering detailed chemistry and transport which are conducted for IPF and OPF in an iso-octane/air mixture at different initial temperatures and pressures. Both theoretical and numerical results suggest that compared to infinite number of ignition sparks at side wall, the single central ignition has the advantages in shortening the combustion duration and reducing the tendency of end-gas autoignition.

Keywords: end-gas autoignition; ignition configuration; flame propagation; iso-octane/air

1. Introduction

Due to the stringent regulations on engine emission and fuel consumption, many advanced combustion technologies have been proposed for spark ignition engines (SIEs) recently [1]. Downsized and in-take boosted direct-injection spark ignition is one of the most promising technologies. However, in highly-boosted SIEs, there is a strong tendency of engine knock, which can cause severe engine damage [2–4].

*Corresponding author. Email: cz@pku.edu.cn

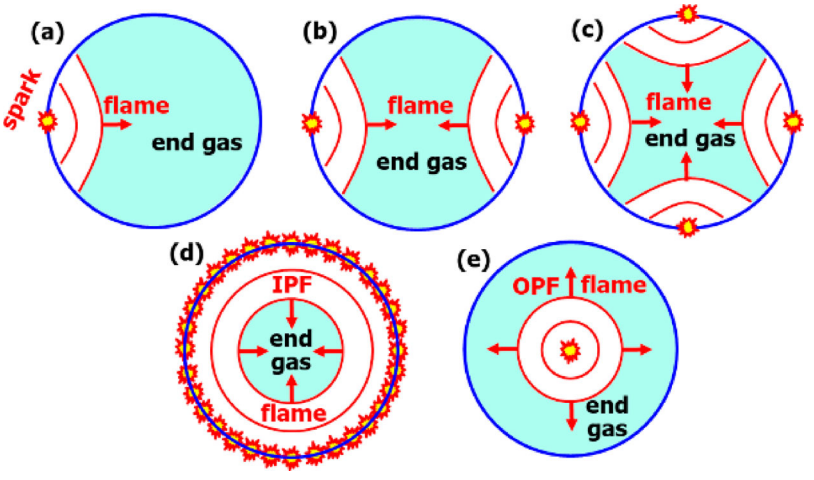

Figure 1. Schematics for different ignition configurations: (a) one-spark, (b) dual-spark, (c) four-spark, (d) infinite number of sparks at side wall, and (e) one central spark. The arrows denote flame propagation direction toward unburned end-gas.

It is generally accepted that engine knock is caused by end-gas autoignition [5–7]. End-gas autoignition occurs when the local ignition delay time at some position(s) in the unburned gas (end-gas), τ_{ig}, is shorter than the time taken by the propagating flame to consume all the unburned mixture, τ_f, (which is referred to as combustion duration since the duration for end-gas autoignition is negligible compared to the duration for flame propagation) [4,8]. In order to prevent knock, we need to make $\tau_{ig} > \tau_f$ via changing τ_{ig} or/and τ_f. As reviewed by Wang et al. [4] there are different knock control strategies including retarding spark timing, increasing octane number, exhaust gas recirculation, mixture stratification, etc. This study focuses on ignition configuration which can change the combustion duration, τ_f, and end-gas autoignition and thereby can be used for knock control [9].

Recently, multiple spark ignition has received great attention due to the facts that it can shorten combustion duration and thereby increase the engine thermal efficiency [10] and that it can extend the lean-burn limit and reduce misfire in SIEs [11]. Different from traditional one-spark ignition system (Figure 1(a) and (e)), in multiple ignition system two or more spark plugs are used as sketched in Figure 1(b) and 1 (c). In the literature, there are several studies on how the ignition configuration affects engine knock. The simulations and experiments respectively conducted by Pasternak et al. [12] and Chen et al. [13] both showed that engine knock is more prone to occur with dual/multiple spark than a single spark. However, Kartha et al. [14] found that multiple spark ignition can mitigate knock severity. Liu et al. [9] investigated the influence of ignition configuration on knock using an optical rapid compression machine. They found that the knock intensity changes non-monotonically with the spark plug number. Similar trend was also observed in experiments by Shi et al. [15–17], who investigated the knock characteristics under different spark strategies (e.g. spark number and location) in a single-cylinder optical research engine. They found that the knock intensity first increases as the number of active sparks goes from one to three and then decreases significantly with four-spark ignition. The different trends observed in these studies [9,12–17] indicate that there is still an incomplete understanding of how the ignition configuration affects knock. This motivates the current work.

The objective of this study is to assess and interpret the flame propagation direction induced by different ignition configurations on combustion duration and end-gas autoignition. In order to provide general results and to reveal the main physical mechanisms, theoretical analysis considering global one-step chemistry is conducted in Section 2. In order to validate the theoretical results, transient numerical simulations considering complex chemistry and transport are also conducted and the results are presented in Section 3.

To make the theoretical analysis tractable, we consider two simplified ignition configurations. One is with infinite number of spark at the side circular wall (see Figure 1(d)), which mimics the multiple ignition in the experiments [9] and induces an inwardly propagating flame (IPF). The other is with a single central spark (see Figure 1(e)), which induces an outwardly propagating flame (OPF). Obviously, the combustion duration decreases as the number of sparks increases, i.e. from (a) to (d) in Figure 1. However, it is not straightforward to know whether the combustion duration of IPF in Figure 1(d) is shorter than that of OPF in Figure 1(e). In the following, the one-dimensional (1D) IPF and OPF with and without end-gas autoignition in a closed cylindrical chamber are investigated. It is noted that in practice, it is impossible to have infinite number of spark at the side wall as shown in Figure 1(d) and the flame is not one-dimensional. The IPF is a model to investigate the multiple spark ignition method. When the spark number near the wall is infinite, it can be treated as a hot ring-shaped region. Nevertheless, the 1D IPF and OPF induced by the ignition configuration in Figure 1(d) and 1 (e) provide idealised models which can be used to show the effects of flame propagation direction on combustion duration and end-gas autoignition. Note that the ignition setup for IPF is not feasible in practice. This idealised ignition setup is chosen so that 1D flame propagation can be achieved and analysed/simulated. The present 1D theory and simulation cannot handle finite number of spark as shown in Figure 1(b) and 1 (c) since the corresponding flame front is multi-dimensional.

2. Theoretical analysis

2.1. *Formulations and analytical solutions*

The 1D OPF with end-gas autoignition in a closed chamber was analysed by Kagan et al. [18,19] and Yu et al. [20]. For IPF, it is straightforward to conduct similar analysis though there is no such theoretical study in the literature. The governing equations for IPF and OPF are the same though the flame propagation direction is different. The equations and analytical solutions for OPF with end-gas autoignition in planar geometry were presented in [19]. Following [19], here we obtain the equations and analytical solutions for 1D IPF and OPF in a cylindrical coordinate. In the following, we briefly present the governing equations and analytical solutions for 1D IPF with end-gas autoignition. The detailed derivation for both IPF and OPF is provided in the Supplementary Document.

The non-dimensional governing equations for normalised temperature, T, mass fraction of deficient reactant, C, and mass conservation together with the equations of state and chemical reaction rate of one-step chemistry are [19]:

$$\rho\left(\frac{\partial T}{\partial t}+u\frac{\partial T}{\partial r}\right)=\varepsilon\frac{1}{r}\frac{\partial}{\partial r}\left(r\frac{\partial T}{\partial r}\right)+\frac{\gamma-1}{\gamma}\frac{dP}{dt}+\frac{1}{\varepsilon}(1-\sigma)W \tag{1}$$

$$\rho\left(\frac{\partial C}{\partial t}+u\frac{\partial C}{\partial r}\right)=\frac{\varepsilon}{Le}\frac{1}{r}\frac{\partial}{\partial r}\left(r\frac{\partial C}{\partial r}\right)-\frac{1}{\varepsilon}W \tag{2}$$

$$\frac{\partial \rho}{\partial t} + \frac{1}{r}\frac{\partial}{\partial r}(r\rho u) = 0 \tag{3}$$

$$P = \rho T, P = P(t) \tag{4}$$

$$W = Z\rho C exp(N(1 - T^{-1})) \tag{5}$$

where P, ρ and u denote the scaled pressure, density, temperature and velocity, respectively; r and t, the scaled spatial coordinate and time, respectively; Le, the Lewis number; $N = T_a/T_b$, the scaled activation temperature in the unit of adiabatic flame temperature T_b; and $\sigma = T_0/T_b$, the scaled initial temperature. The non-dimensional process is shown in The small parameter used later for asymptotic analysis is $\varepsilon = l_{th}/R_W$, which is the scaled flame width by the inner radius of the cylindrical chamber, R_W. The parameter $Z = (2Le)^{-1}N^2(1\text{-}\sigma)^2$ is a normalised factor [19]. Note that all variables are scaled in the same manner as Ref. [19]. The details on the non-dimensional process are shown in the Supplementary Document. Here we only consider unit Lewis number (i.e. $Le = 1$) since the analytical solutions might not be obtained for non-unity Lewis number. For lean hydrogen combustion with $Le < 1$, the positive and negative stretch of OPF and IPF has opposite effects on the propagation speed and flame strength and thereby it is important to consider the Lewis number effect. Further efforts need to be devoted to extending the present theory for non-unity Lewis numbers in future works.

Note that here we consider the first-order global reaction. When a second-order global reaction is considered, the reaction rate in Equation (5) will be proportional to the square of the density. Therefore, quantitative influence by the reaction order on the results is expected. Nevertheless, only quantitative prediction for theoretical analysis is expected. The good agreement between the theoretical analysis and numerical simulations considering detailed chemistry in predicting the occurrence of end-gas autoignition has clearly demonstrated the rationality of the simple Arrhenius-type kinetics that only considers the deficient species.

Under low Mach number approximation, the pressure only changes with time and is independent of the spatial coordinate [21]. In the unburned zone, $0 < r < R_f$ (where R_f is the flame radius) of the IPF, T, C and ρ are independent of the spatial coordinate r and only changes with time, t. Therefore, the governing equations for the unburned zone ($0 < r < R_f$) reduce to [19]

$$\rho_+ \frac{\partial T_+}{\partial t} = \frac{\gamma - 1}{\gamma}\frac{dP}{dt} + \frac{1}{\varepsilon}(1 - \sigma)W_+ \tag{6}$$

$$\rho_+ \frac{\partial C_+}{\partial t} = -\frac{1}{\varepsilon}W_+ \tag{7}$$

$$\frac{\partial \rho_+}{\partial t} + \frac{1}{r}\frac{\partial}{\partial r}(r\rho_+ u_+) = 0 \tag{8}$$

$$P = \rho_+ T_+, P = P(t) \tag{9}$$

$$W_+ = Z\rho_+ C_+ \exp(N(1 - T_+^{-1})) \tag{10}$$

The subscripts + and – denote states for unburned and burned zones, respectively. Note that the consumption of the unburned reactant is considered in Equation (7) and C_+ decreases when chemical reaction due to autoignition occurs in the unburned zone. Besides, the ignition delay of unburned gas is implicitly included by considering the chemical reaction in the unburned gas region according to Equations (6) and (7).

In the burned zone, $R_f < r < 1$ (note that r is scaled by the inner radius of the cylindrical chamber and thus $r = 1$ corresponds to the wall), we have $C = 0$ and thereby zero reaction rate. Consequently, the governing equations for the burned zone do not have the source term for chemical reaction and reduce to

$$\rho_- \left(\frac{\partial T_-}{\partial t} + u_- \frac{\partial T_-}{\partial r} \right) = \frac{\gamma - 1}{\gamma} \frac{dP}{dt} \tag{11}$$

$$\frac{d\rho_-}{dt} + \frac{1}{r} \frac{d}{dr}(r\rho_- u_-) = 0 \tag{12}$$

$$P = \rho_- T_-, P = P(t) \tag{13}$$

Adiabatic wall is considered here. Therefore, at both boundaries at $r = 0$ and $r = 1$, the spatial derivatives for T and C are always zero. Note that the heat transfer near the wall does affect the autoignition in unburned gas [7]. The end-gas autoignition in IPF is not affected by heat loss on the wall. Therefore, we should also consider the end-gas autoignition in OPF without wall heat loss so that the comparison between IPF and OPF is reasonable. Besides, the velocity at both boundaries is also always zero, i.e.

$$u_+(0, t) = 0, u_-(1, t) = 0 \tag{14}$$

The initial conditions are

$$T_-(r, 0) = 1, T_+(0) = \sigma$$

$$u_-(r, 0) = 0, u_+(0) = 0$$

$$\rho_-(r, 0) = 1, \rho_+(0) = 1/\sigma$$

$$C_+(r, 0) = 1, P(0) = 1, R_f(0) = 1 \tag{15}$$

Across the flame front, $r = R_f$, the mass flux continuity and enthalpy flux continuity should be ensured, which yields the following matching conditions [19]

$$\rho_+ \left(\frac{dR_f}{dt} - u_+ \right) = \rho_- \left(\frac{dR_f}{dt} - u_- \right) = -\lambda \tag{16}$$

$$T_- = T_+ + (1 - \sigma) C_+ \tag{17}$$

Following [19], we introduce the stretched spatial coordinate, η, which is attached to the moving flame front, $R_f = R_f(t)$,

$$\eta = [r - R_f(t)]/\varepsilon \tag{18}$$

where $\varepsilon = l_{th}/R_W$ is ratio between flame width and inner radius of the chamber. In the stretched coordinate and in the asymptotic limit of $\varepsilon >> 1$, the governing Equations (1) and (2) in the leading order are

$$\lambda \frac{\partial T}{\partial \eta} = \frac{\partial^2 T}{\partial \eta^2} + (1 - \sigma) W \tag{19}$$

$$\lambda \frac{\partial C}{\partial \eta} = \frac{1}{Le} \frac{\partial^2 C}{\partial \eta^2} - W \tag{20}$$

The boundary conditions obtained from matching inner and outer solutions are:

$$T(\eta = -\infty) = T_+, T(\eta = +\infty) = T_-(r = R), \\ C(\eta = -\infty) = C_+, C(\eta = +\infty) = 0\# \tag{21}$$

The eigenvalue problem described by the above Equations (19)–(21) is the same as the adiabatic planar flames and can be solved via the classical large-activation-asymptotic analysis with $N >> 1$ [21]. The following expression for λ can be derived (see the detailed derivation in the Supplementary Document)

$$\lambda = \left(\frac{T_-^2}{C_+}\right)\left(\frac{P}{T_-}\right)^{\frac{1}{2}} \exp\left[\frac{N}{2}\left(\frac{T_- - 1}{T_-}\right)\right] \tag{22}$$

Note that the flame speed is not an eigenvalue since there is chemical reaction/autoignition in the unburned mixture. Recently, there have been many studies [22–24] on the flame speed of autoignition-assisted flame. Equation (22) shows that when the fuel in the 'unburned' mixture is close to zero, $C_+ = 0$, the flame speed approaches infinity. This is consistent with previous simulation and theoretical results on autoignition-assisted premixed flame. Nevertheless, more efforts need to be devoted to theoretical analysis of laminar flame speed of autoignition-assisted premixed flame.

The expressions from velocity at burned and unburned zones can be derived from continuity equation and the equation for temperature:

$$u_+ = -\frac{r}{2}\left[\frac{1}{\gamma}\frac{d(\ln P)}{dt} - \frac{(1-\sigma)W_+}{\varepsilon P}\right], 0 < r < R_f \tag{23}$$

$$u_- = \frac{1}{2}\left(\frac{1}{r} - r\right)\frac{d\left(\ln P^{\frac{1}{\gamma}}\right)}{dt}, R_f < r < 1 \tag{24}$$

By using continuity equation and some algebra rearrangements, we can get

$$P = P_e T_+ / [T_+ + \sigma(P_e - 1)C_+ R_f^2] \tag{25}$$

$$\frac{dR_f}{dt} = -\lambda\left(\frac{T_-}{P}\right) + \frac{1}{2}\left(\frac{1}{R_f} - R_f\right)\frac{1}{\gamma}\frac{1}{P}\frac{dP}{dt} \tag{26}$$

To calculate the temperature profiles in the burned zone, we need consider the scaled entropy, S, which is controlled by entropy balance [17]:

$$\frac{\partial S_-}{\partial t} + u_-\frac{\partial S_-}{\partial r} = 0 \,\text{with} S_- = \ln\left(P^{\frac{1-\gamma}{\gamma}} T_-\right) \tag{27}$$

The above equation can be solved analytically (see the Supplementary Document), and according to the relationship between S and T- in Equation (27), we have the following expression for temperature distribution in the burned zone

$$T_-(r,t) = P^{\frac{\gamma-1}{\gamma}} \exp\left(F\left(P^{\frac{1}{\gamma}}(1 - r^2)\right)\right) \tag{28}$$

Similar analysis can be conducted for the 1D OPF with end-gas autoignition in a closed cylindrical chamber. The details are shown in the Supplementary Document.

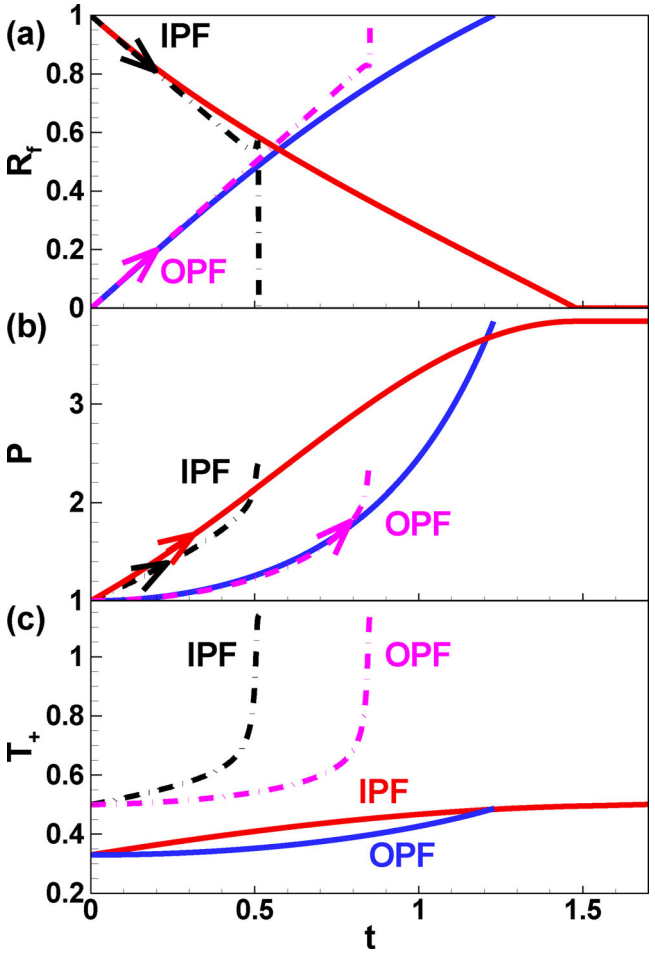

Figure 2. Evolution of (a) flame radius, (b) pressure and (c) temperature of unburned gas for OPF and IPF at $\sigma = 0.33$ (solid lines, without end-gas autoignition) and $\sigma = 0.5$ (dash-dotted lines, with end-gas autoignition).

Here we consider the fixed parameters of $\gamma = 1.4$, $Le = 1$ and $N = 9$. The temporal evolutions of flame radius and pressure can be obtained by solving Equations (6), (7), (26), (13), (9), (17), (22) and (25). Then the velocity and temperature distributions can be obtained from Equations (23), (24) and (28). The results obtained from solving these equations are presented in the next subsection.

2.2. *Theoretical results and discussion*

End-gas autoignition can be induced by increasing either the chamber radius (i.e. to increase τ_f) or the initial temperature (i.e. to decrease τ_{ig}) [25]. Unlike [19], here we fix chamber radius and fix $\varepsilon = 0.05$ which is inversely proportional to the chamber radius. We change the initial temperature and thereby change the ratio between the initial temperature and adiabatic flame temperature, σ. The results for OPF and IPF at $\sigma = 0.33$ and $\sigma = 0.5$ corresponding to two different initial temperatures are shown in Figure 2.

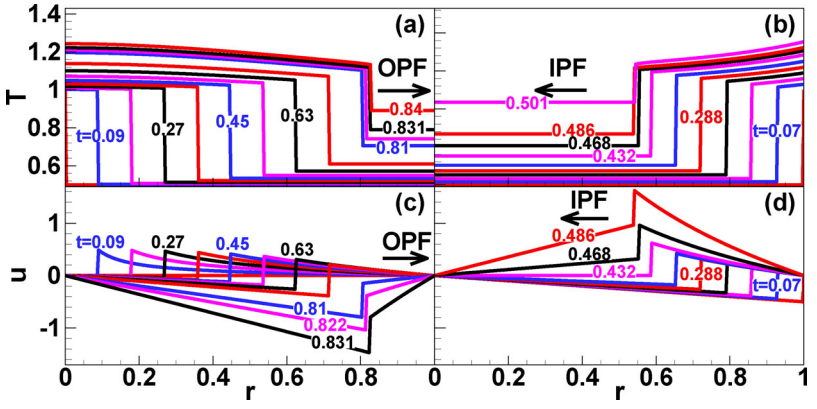

Figure 3. Temporal evolution of temperature and flow velocity distributions for OPF/IPF with end-gas autoignition, $\sigma = 0.5$. The corresponding instants for several lines are marked.

Figure 2 shows when the initial temperature increases from $\sigma = 0.33$ to $\sigma = 0.5$, end-gas autoignition occurs, which results in the abrupt increase in both the pressure and temperature of the unburned gas. For $\sigma = 0.33$ without end-gas autoignition, Figure 2 shows that the combustion duration of OPF is shorter than that of IPF, i.e. $\tau_{f,OPF} < \tau_{f,IPF}$. This means that, counterintuitively, the infinite number of sparks at the side wall in Figure 1(d) corresponds to longer combustion duration than the single central ignition in Figure 1(e). This counterintuitive observation of $\tau_{f,OPF} < \tau_{f,IPF}$ shall be explained later.

Figure 2(b) shows that for OPF with $\sigma = 0.33$, the pressure first slightly rises and then rises quickly as the flame approaches the wall. However, the pressure in IPF first increases in a nearly linear manner for a long duration. This can be explained by the change of flame surface area and burning rate. The flame surface area of OPF increases with time, while the opposite holds for IPF. For both OPF and IPF, the burning rate increases with time since the temperature of unburned gas increases due to compression. Consequently, both factors accelerate pressure rise in OPF; while these two factors have opposite effect on pressure rise in IPF, resulting in a nearly linear pressure rise in IPF.

Figure 2(b) and 2 (c) show at the same initial temperature, the pressure and temperature of unburned end gas for IPF are higher than those for OPF, indicating $\tau_{ig,IPF} < \tau_{ig,OPF}$. As mentioned before, we have $\tau_{f,IPF} > \tau_{f,OPF}$. Consequently, Figure 2 shows that end-gas autoignition (happening under the condition that $\tau_{ig} < \tau_f$) is more prone to occur in IPF than in OPF. This means that, compared to the infinite number of sparks at side wall in Figure 1(d), the single central ignition in Figure 1(e) helps to mitigate knock severity.

Figure 3 shows the evolution of temperature and flow velocity distributions for OPF and IPF with end-gas autoignition. Before end-gas autoignition occurs, the temperature of unburned gas gradually increases since it is compressed by the propagating flame. Figure 3(c) shows that inward flow appears in the burned gas of OPF. Such inward flow has large impact on laminar flame speed measured from spherical OPF (see [26] and references therein). When autoignition occurs in OPF, the intensive heat release from global end-gas autoignition significantly increases the inward flow velocity and thereby induces backward motion of the flame front. For IPF, the flow is shown to be in the opposite direction to that for OPF. This is reasonable since the flow is mainly induced by the thermal expansion and the flow direction is mainly by the direction of flame propagation. Furthermore, Figure

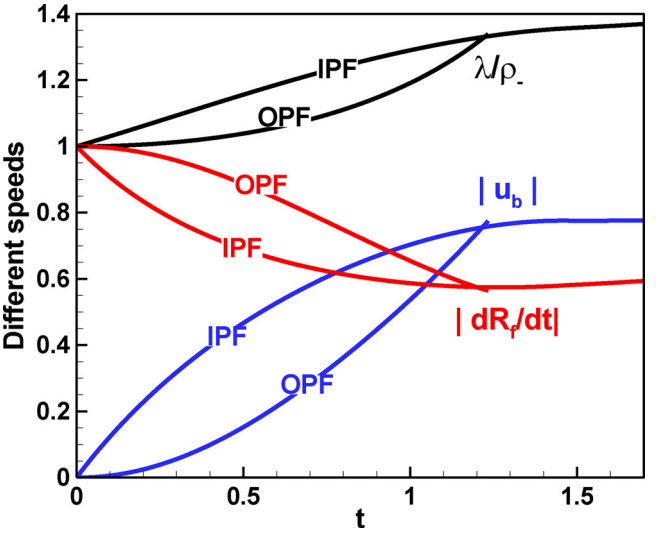

Figure 4. Change of different speeds with time for OPF and IPF without end-gas autoignition, $\sigma = 0.33$.

3(a) and 3 (b) show that the burned gas temperature is not uniform. This is due to the Mach effect [27].

In order to explain why the combustion duration of OPF is shorter than that of IPF, we analyse the different terms of the absolute flame propagation speed, $|dR_f\ /dt|$. For both OPF and IPF, we have:

$$\left|\frac{dR_f}{dt}\right| = \frac{\lambda}{\rho_-} - |u_b| \tag{30}$$

where λ/ρ_- is the laminar flame speed relative to the burned gas, and $|u_b|$ is the flow speed of burned gas at the flame front. The temporal evolution of these speeds is compared in Figure 4 for OPF and IPF without end-gas autoignition. Overall, the absolute flame propagation speed, $|dR_f\ /dt|$, of OPF is always higher than that of IPF, which results in shorter combustion duration of OPF. Figure 4 shows that the laminar flame speeds relative to the burned gas, λ/ρ_-, for OPF and IPF are close and the value for IPF is slightly larger than that for OPF. However, the absolute value of the flow speed of burned gas close to the flame front, $|u_b|$, for OPF is shown to be much lower than that for IPF. Note that the burned gas flow speed is in the opposite direction to the propagating flame front (see Figure 3). Therefore, it is the difference in the flow speed of burned gas induced by thermal expansion in OPF and IPF that makes the combustion duration of OPF shorter than that of IPF.

The above theoretical analysis indicates that compared to multiple ignitions at side wall (Figure 1(b)–(d)), the single central ignition (Figure 1(e)) has the advantage in reducing combustion duration and engine knock.

The theory is based on one-step chemistry. However, complex chemistry is involved in the combustion of large hydrocarbon fuels used in SIEs. Therefore, in the following, simulations considering complex chemistry are performed for OPF and IPF.

3. Numerical simulations

3.1. *Numerical model and methods*

The model considered in simulations is the same as that in theoretical analysis, i.e. the OPF in Figure 1(e) and IPF in Figure 1(d), respectively, induced by the central ignition and infinite number of sparks at the side circular wall. The chamber radius is fixed to be $R_W = 4$ cm. A hot spot at 1800 K and in the radius of 0.05 mm is used to initiate the OPF, while a hot ring-shaped region ($T = 1800$ K and thickness is 0.05 mm) near the wall is used to initiate the IPF. We consider a stoichiometric iC_8H_{18}/air mixture at three sets of initial temperature and pressure, (450 K, 4.29 atm), (500 K, 6.59 atm) and (650 K, 20 atm), which satisfy the isentropic compression relationship. These three conditions represent different stages of compression in the rapid compression machine and the last condition is close to the engine operating condition. After ignition the pressure and temperature changes in the closed chamber are caused by chemical reactions and moving mesh method is not considered in the simulations.

The transient flame propagation and end-gas autoignition processes are simulated using the in-house code A-SURF [28–30]. It solves the conservation equations for 1D reactive flow in a cylindrical coordinate by the finite volume method. A-SURF has been successfully used in our previous studies on ignition, flame propagation and end-gas autoignition [20,25,31–33]. The details on the governing equations, numerical methods and code validation are presented in [20,28–30] and thereby are not repeated here.

The present numerical setup is nearly the same as that in [20]. The boundary conditions at both $r = 0$ and $r = R_W$ are zero flow speed and zero gradients of temperature and mass fractions of all species (i.e. adiabatic wall). To accurately resolve the flame propagation, locally adaptive mesh refinement is used and the reaction front is always covered by the finest mesh with $\Delta r = 6$ μm. Figure S1 in the Supplementary Document demonstrates that grid independence is achieved. The skeletal mechanism for iC_8H_{18} developed and validated by Wang et al. [34] is used. It consists of 73 species and 296 elementary reactions and was shown to be able to accurately predict flame propagation and multi-stage autoignition [34].

3.2. *Numerical results and discussion*

Figure 5 shows the evolutions of temperature distributions for OPF and IPF at different initial temperatures and pressures: (450 K, 4.29 atm), (500 K, 6.59 atm) and (650 K, 20 atm). For OPF, end-gas autoignition does not occur at $T_0 = 450$ and 500 K while it occurs at $T_0 = 600$ K. This is consistent with the above theoretical results that increasing the initial temperature can induce end-gas autoignition. The time sequences for temperature distributions during autoignition are marked from t_5 to t_{10} in Figure 5(c).

Similarly, Figure 5(d)–(f) shows that increasing the initial temperature can also promote end-gas autoignition in IPF. It is noted that at the same initial temperature of $T_0 = 500$ K, end-gas autoignition does not occur for OPF (see Figure 5(b)) while it occurs for IPF (see Figure 5(e)). Moreover, Figure 5(c) and 5 (f) show that at $T_0 = 650$ K, end-gas autoignition occurs for both OPF and IPF and it happens earlier for IPF than for OPF. These observations are consistent with theory that end-gas autoignition is more prone to occur in IPF than in OPF.

It is noticed that for OPF, Figure 5(c) shows the autoignition starts near the flame front and it propagates toward the wall. However, for IPF Figure 5(f) shows that the autoignition

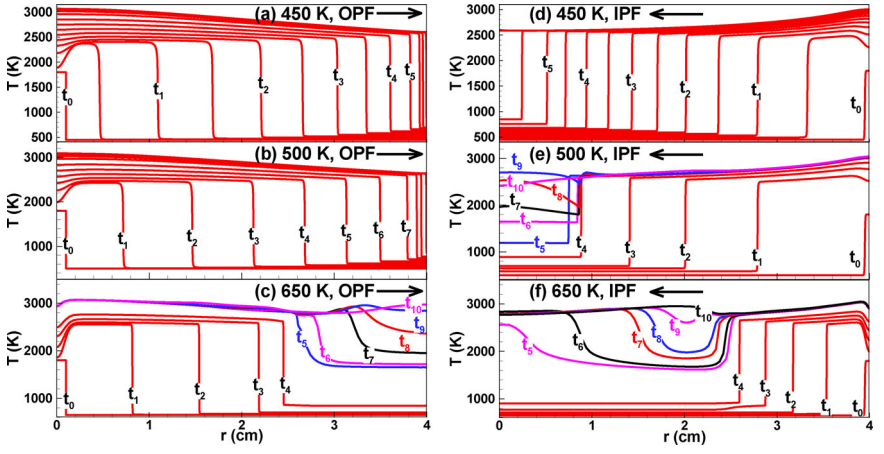

Figure 5. Temporal evolution of temperature distributions for OPF and IPF in a stoichiometric iC_8H_{18}/air mixture at different initial temperatures and pressures.

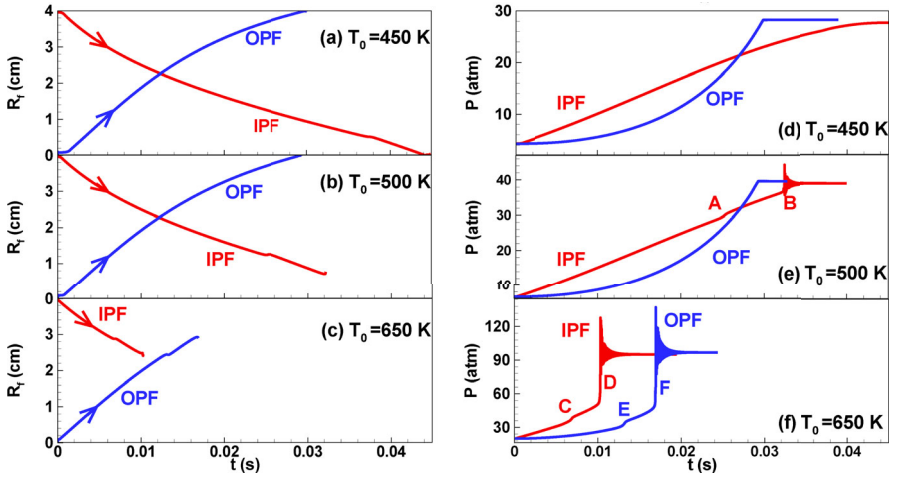

Figure 6. Temporal evolution of flame radius and pressure for OPF and IPF in a stoichiometric iC_8H_{18}/air mixture at different initial temperatures and pressures.

starts at the centre and it propagates toward the flame. This is due to focusing and reflecting of the strong pressure wave in IPF.

To quantify and compare the combustion duration of OPF and IPF, we plot the temporal evolutions of flame radius, R_f, and pressure near the wall, P, in Figure 6. The flame radius is defined based on the location where the maximum heat release appears. Figure 5(a) shows for $T_0 = 450$ K without end-gas autoignition, the combustion duration of OPF is shorter than that of IPF. However, for $T_0 = 650$ K with end-gas autoignition, the combustion duration of OPF is longer than that of IPF. This is because end-gas autoignition is more prone to occur in IPF than OPF and autoignition can greatly reduce the combustion duration. These results agree with the theoretical results shown in Figure 2(a), and thereby demonstrate the validity of theoretical analysis.

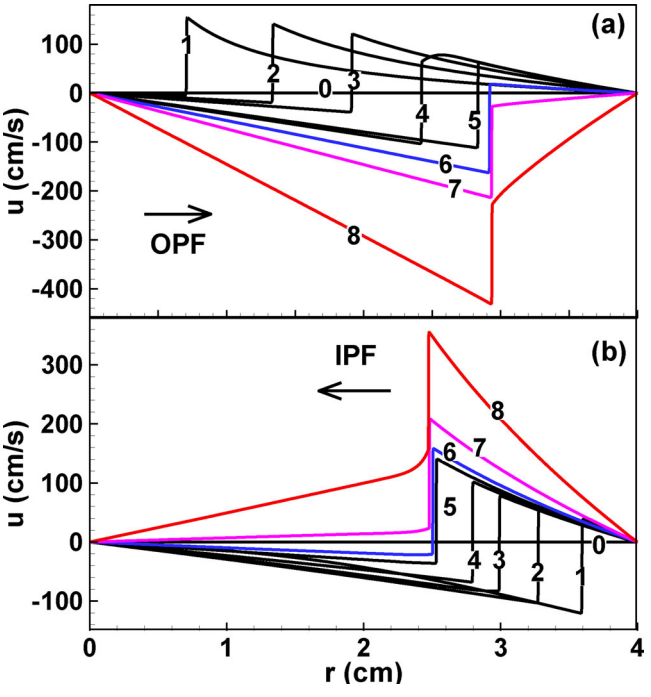

Figure 7. Temporal evolution of velocity distributions for OPF and IPF in a stoichiometric iC_8H_{18}/air mixture initially at 650 K and 20 atm. Line #0 corresponds to $t = 0$ ms, and the time increases from line #1 to line #8.

Figure 6(d)–(f) compares the pressure history for OPF and IPF. The shape of these curves is similar to those shown in Figure 2(b) from theoretical analysis. Unlike theoretical results, strong pressure oscillation (with the amplitude in the order of 10 atm) is observed around points B, D, and F in Figure 6 for cases with end-gas autoignition occurs. It is noted that around points A, C and E in Figure 6, there is slight pressure rise. This is caused by the first-stage autoignition in the end-gas, which cannot be predicted by theoretical analysis. Nevertheless, the theory can capture the main physics and provide more general results/conclusions than simulations.

Figure 7 plots the evolution of flow velocity distributions for OPF and IPF with end-gas autoignition. The black lines correspond to normal flame propagation while the coloured lines correspond to the times when autoignition already occurs. For both OPF and IPF, the flow velocities change abruptly across the flame front, and autoignition can greatly increase the magnitude of flow velocity. This is due to the intensive heat release from global end-gas autoignition. The simulation results in Figure 7 agree, at least qualitatively, with the theoretical prediction shown in Figure 3.

4. Conclusions

Asymptotic theoretical analysis and transient simulations are conducted to assess the effects of flame propagation direction on combustion duration and end-gas autoignition. The OPF and IPF, respectively induced by the central spark and infinite number of sparks at the side circular wall in a closed cylindrical chamber are investigated.

The temporal evolution of flame front position, unburned gas temperature and pressure as well as the distributions of temperature and flow velocity are obtained from theoretical analysis. As expected, it is found that end-gas autoignition can be induced by increasing the initial temperature. Counterintuitively, the combustion duration of OPF is found to be shorter than that of IPF when there is no end-gas autoignition. This counterintuitive observation is mainly due to the difference in the flow speed of burned gas induced by the thermal expansion in OPF and IPF. However, when end-gas autoignition occurs, the combustion duration of IPF is shorter than that of OPF. Furthermore, it is shown that the end-gas autoignition is more prone to occur in IPF than OPF. This is attributed to the larger flame front surface from the early stage for IPF, which leads to a faster increase in temperature and pressure of unburned end gas than OPF.

To validate the theoretical analysis, transient simulations considering detailed chemistry and transport are conducted for IPF and OPF in a stoichiometric iso-octane/air mixture. The first-stage autoignition in the end-gas is demonstrated to cause a slight pressure rise, which cannot be predicted by theoretical analysis. Nevertheless, the theory can capture the main physics and provide more general results/conclusions than simulations. Both theoretical and numerical results suggest that compared to infinite number of ignition sparks at side wall, the single central ignition has the advantage in reducing combustion duration and engine knock.

It is noted that for the sake of analytical tractability, this work considers the idealised ignition configurations shown in Figure 1(d) and 1 (e), for which one-dimensional IPF and OPF can be induced. Only one-dimensional analysis and simulations need to be conducted for IPF and OPF shown in Figure 1(d) and 1 (e). In future works, it would be interesting consider the ignition configurations shown in Figure 1(a)–(c), for which multi-dimensional simulations need to be conducted. Besides, in practical engines, the flame propagation and end-gas autoignition are strongly affected by turbulence [35–37] and thereby it would be interesting to take into account turbulence effects. Besides, the heat transfer from wall and piston movement need also to be considered in order to represent realistic engine operating conditions.

Disclosure statement

No potential conflict of interest was reported by the author(s).

Supplemental data

Supplemental data for this article can be accessed at https://doi.org/10.1080/13647830.2022.2153741.

Funding

This work was supported by the National Natural Science Foundation of China [grant number 52176096].

ORCID

Zheng Chen http://orcid.org/0000-0001-7341-6099

References

[1] R. Reitz, *Directions in internal combustion engine research*. Combust. Flame 160 (2013), pp. 1–8.

[2] X. Zhen, Y. Wang, S. Xu, Y. Zhu, C. Tao, T. Xu and M. Song, *The engine knock analysis – An overview*. Appl. Energy 92 (2012), pp. 628–636.

[3] E. Galloni, *Dynamic knock detection and quantification in a spark ignition engine by means of a pressure based method*. Energy Convers. Manage 64 (2012), pp. 256–262.

[4] Z. Wang, H. Liu and R.D. Reitz, *Knocking combustion in spark-ignition engines*. Prog. Energy Combust. Sci 61 (2017), pp. 78–112.

[5] J.B. Heywood, *Internal Combustion Engine Fundamentals*, 1st ed., McGraw-Hill Education, New York, 1988.

[6] J. Pan, G. Shu and H. Wei, *Interaction of flame propagation and pressure waves during knocking combustion in spark-ignition engines*. Combust. Sci. Technol 186 (2014), pp. 192–209.

[7] H. Terashima and M. Koshi, *Mechanisms of strong pressure wave generation in end-gas autoignition during knocking combustion*. Combust. Flame 162 (2015), pp. 1944–1956.

[8] J.C. Livengood and P.C. Wu, *Correlation of autoignition phenomena in internal combustion engines and rapid compression machines*. Symposium (International) on Combustion 5 (1955), pp. 347–356.

[9] W. Liu, Y. Qi, X. He and Z. Wang, *Investigation on effects of ignition configurations on knocking combustion using an optical rapid compression machine under lean to stoichiometric conditions*. Combust. Sci. Technol (2020), pp. 1–22.

[10] İ Altın and A. Bilgin, *Quasi-dimensional modeling of a fast-burn combustion dual-plug spark-ignition engine with complex combustion chamber geometries*. Appl. Therm. Eng 87 (2015), pp. 678–687.

[11] Y. Takashima, H. Tanaka, and T. Sako, Evaluation of the effects of combustion by multi-ignition in natural gas engines, SAE Technical Paper 2012-32-0065, 2012.

[12] M. Pasternak, F. Mauss, F. Xavier, M. Rieß, M. Sens, and A. Benz, 0D/3D Simulations of Combustion in Gasoline Engines Operated with Multiple Spark Plug Technology, SAE Technical Paper 2015-01-1243, 2015.

[13] L. Chen, J. Pan, C. Liu, G. Shu and H. Wei, *Effect of rapid combustion on engine performance and knocking characteristics under different spark strategy conditions*. Energy 192 (2020), pp. 116706.

[14] B.N. Kartha, S. Vijaykumar, and P. Reddemreddy, Thermodynamic split of losses analysis of a single cylinder gasoline engine with multiple spark plug – ignition coil configurations, SAE Technical Paper 2016-32-0008, 2016.

[15] H. Shi, Q. Tang, K. Uddeen, G. Magnotti and J. Turner, *Optical diagnostics and multi-point pressure sensing on the knocking combustion with multiple spark ignition*. Combust. Flame 236 (2022), pp. 111802.

[16] H. Shi, Q. Tang, K. Uddeen, B. Johansson, J. Turner and G. Magnotti, *Effects of multiple spark ignition on engine knock under different compression ratio and fuel octane number conditions*. Fuel 310 (2022), pp. 122471.

[17] H. Shi, K. Uddeen, Y. An, and B. Johansson, Experimental study on knock mechanism with multiple spark plugs and multiple pressure sensors, SAE Technical Paper 2020-01-2055, 2020.

[18] L.S. Kagan, P.V. Gordon and G.I. Sivashinsky, *A minimal model for end-gas autoignition*. Combust. Theor. Model 16 (2012), pp. 1–12.

[19] L. Kagan and G. Sivashinsky, *Hydrodynamic aspects of end-gas autoignition*. Proc. Combust. Inst 34 (2013), pp. 857–863.

[20] H. Yu, C. Qi and Z. Chen, *Effects of flame propagation speed and chamber size on end-gas autoignition*. Proc. Combust. Inst 36 (2017), pp. 3533–3541.

[21] C.K. Law, *Combustion Physics*, Cambridge University Press, Cambridge, 2006.

[22] A. Krisman, E.R. Hawkes and J.H. Chen, *The structure and propagation of laminar flames under autoignitive conditions*. Combust. Flame 188 (2018), pp. 399–411.

[23] M. Faghih, H. Li, X. Gou and Z. Chen, *On laminar premixed flame propagating into autoigniting mixtures under engine-relevant conditions*. Proc. Combust. Inst 37 (2019), pp. 4673–4680.

[24] T. Zhang and Y. Ju, *Structures and propagation speeds of autoignition-assisted premixed n-heptane/air cool and warm flames at elevated temperatures and pressures*. Combust. Flame 211 (2020), pp. 8–17.
[25] H. Yu and Z. Chen, *End-gas autoignition and detonation development in a closed chamber*. Combust. Flame 162 (2015), pp. 4102–4111.
[26] Z. Chen, *On the accuracy of laminar flame speeds measured from outwardly propagating spherical flames: Methane/air at normal temperature and pressure*. Combust. Flame 162 (2015), pp. 2442–2453.
[27] B. Lewis and G. Elbe, *Combustion, Flames and Explosions of Gases*, Third ed., Elsevier, 1987.
[28] P. Dai and Z. Chen, *Supersonic reaction front propagation initiated by a hot spot in n -heptane/air mixture with multistage ignition*. Combust. Flame 162 (2015), pp. 4183–4193.
[29] Z. Chen, M.P. Burke and Y. Ju, *Effects of Lewis number and ignition energy on the determination of laminar flame speed using propagating spherical flames*. Proc. Combust. Inst 32 (2009), pp. 1253–1260.
[30] Z. Chen, *Effects of radiation and compression on propagating spherical flames of methane/air mixtures near the lean flammability limit*. Combust. Flame 157 (2010), pp. 2267–2276.
[31] Y. Wang, W. Han and Z. Chen, *Effects of fuel stratification on ignition kernel development and minimum ignition energy of n-decane/air mixtures*. Proc. Combust. Inst 37 (2019), pp. 1623–1630.
[32] Y. Wang, A. Movaghar, Z. Wang, Z. Liu, W. Sun, F.N. Egolfopoulos and Z. Chen, *Laminar flame speeds of methane/air mixtures at engine conditions: Performance of different kinetic models and power-law correlations*. Combust. Flame 218 (2020), pp. 101–108.
[33] X. Chen, H. Böttler, A. Scholtissek, C. Hasse and Z. Chen, *Effects of stretch-chemistry interaction on chemical pathways for strained and curved hydrogen/air premixed flames*. Combust. Flame 232 (2021), pp. 111532.
[34] H. Wang, M. Yao and R.D. Reitz, *Development of a reduced primary reference fuel mechanism for internal combustion engine combustion simulations*. Energy Fuels 27 (2013), pp. 7843–7853.
[35] F. Zhang, R. Yu and X.S. Bai, *Direct numerical simulation of PRF70/air partially premixed combustion under IC engine conditions*. Proc. Combust. Inst 35 (2015), pp. 2975–2982.
[36] M.B. Luong, F.E. Hernández Pérez and H.G. Im, *Prediction of ignition modes of NTC-fuel/air mixtures with temperature and concentration fluctuations*. Combust. Flame 213 (2020), pp. 382–393.
[37] M.B. Luong, S. Desai, F.E. Hernández Pérez, R. Sankaran, B. Johansson and H.G. Im, *A statistical analysis of developing knock intensity in a mixture with temperature inhomogeneities*. Proc. Combust. Inst 38 (2021), pp. 5781–5789.